Broadly tunable metal halide perovskites for solid-state light-emission applications

Adjokatse, Sampson; Fang, Hong-Hua; Loi, Maria

Published in:
Materials Today

DOI:
10.1016/j.mattod.2017.03.021

Publication date:
2017

ELSEVIER

Broadly tunable metal halide perovskites for solid-state light-emission applications

Sampson Adjokatse, Hong-Hua Fang* and Maria Antonietta Loi*

Zernike Institute for Advanced Materials, University of Groningen, Nijenborgh 4, Groningen 9747 AG, The Netherlands

The past two years have witnessed heightened interest in metal-halide perovskites as promising optoelectronic materials for solid-state light emitting applications beyond photovoltaics. Metal-halide perovskites are low-cost solution-processable materials with excellent intrinsic properties such as broad tunability of bandgap, defect tolerance, high photoluminescence quantum efficiency and high emission color purity (narrow full-width at half maximum). In this review, the photophysical properties of hybrid perovskites, which relates with light-emission, such as broad tunability, nature of the recombination processes and quantum efficiency are examined. The prospects of hybrid perovskite light-emitting diodes and lasers, and their key challenges are also discussed.

Introduction

Solid-state light-emitting devices such as light-emitting diodes (LEDs) and lasers play important roles in modern day life. They have the potential to address urgent challenges not only relating to general lighting and display applications but also relating to energy saving and greenhouse gas emissions [1]. Through development of materials science, a variety of light emitting materials have been demonstrated since the first demonstration of visible-spectrum LEDs based on gallium arsenide phosphide (GaAsP) over five decades ago [2]. This has led to the evolution of various LED technologies: inorganic semiconductor LEDs [2–7], organic LEDs (OLEDs) [8–11], polymer LEDs (PLEDs) [12,13], quantum-dot LEDs (QLEDs) [14–19] and recently, perovskite LEDs (PeLEDs) [20–27].

Perovskites are a class of compounds that adopts the ABX_3 three-dimensional (3D) structural framework (see Fig. 1a), where A and B are cations of various valence and ionic radii and X is an anion. For metal-halide hybrid perovskites, the A component is usually a monovalent organic cation [typically methylammonium ($CH_3NH_3^+ = MA^+$) or formamidinium ($HC(NH_2)_2^+ = FA^+$)], an atomic cation (typically Cs^+) or a mixture thereof, the B component is often a divalent metal cation (usually Pb^{2+}, Sn^{2+} or a mixture) and X component is a halide anion (typically Cl^-, I^-, Br^- or a mixture thereof) [28–36]. The synthesis of this class of materials is usually performed in solution from which bulk, layered or nanostructured perovskites can be obtained. For example, Liu *et al.* [37] and Shi *et al.* [38] have shown that large-sized perovskite single crystals with dimensions exceeding 10 mm with high crystalline quality can be grown. Figure 1b shows a photograph of a representative $MAPbX_3$ (X = Cl, Br, I) perovskite single crystals grown using a solution method [37]. The substitution of the halogen ion transforms the color of the single crystals from colorless (X = Cl) to orange (X = Br) and then to black (X = I). Mohite and colleagues [39] also demonstrated the formation of continuous perovskite thin films with millimeter-scale crystalline grains that are devoid of pinholes via solution-based hot-casting technique (Fig. 1c). In addition to bulk (single crystals and films) perovskites, nanostructures (quantum dots, nanoplatelets and nanowires) (Fig. 1d) of exceptional photophysical properties have also been reported [40–43].

Hybrid perovskites have demonstrated their superiority in the photovoltaic field as light absorbers with current certified power conversion efficiency (PCE) of 22.1% [44]. They have also shown to have characteristics that are ideal for light emission-based and X-ray detection technology [20,23–26,45–47]. In fact, they exhibit tunable color emission and high quantum efficiency, making them suitable for the fabrication of cheap and green electroluminescent devices. Devices such as light-emitting diodes [20–27], diode lasers [20,45] and light-emitting field-effect transistors [48]

*Corresponding authors:. Fang, H.-H. (H.Fang@rug.nl), Loi, M.A. (M.A.Loi@rug.nl)

 http://dx.doi.org/10.1016/j.mattod.2017.03.021

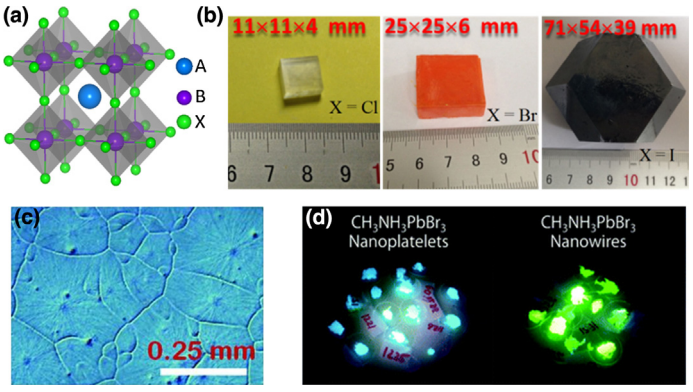

FIGURE 1

(a) Schematic model of the perovskite crystal structure. 'A' represents the organic or inorganic cation, 'B' represents the metal ion, and 'X' represents the halogen ion; (b) photographs taken from the as-grown $CH_3NH_3PbX_3$ crystals. Reprinted with permission from [37]; (c) optical micrograph showing continuous perovskite thin film with millimeter-scale crystalline grains formed via solution-based hot-casting technique [39]. Reprinted with permission from AAAS; (d) photographs of thin films of blue-emitting nanoplatelets and green-emitting nanorods, taken under UV radiation [141]. Reprinted with permission of The Royal Society of Chemistry.

have been demonstrated. The success in the fabrication of these optoelectronic devices has also stimulated the investigation of the photophysics of these materials in different forms, helping to better understand their physical properties and understand the prospective of the materials for optoelectronics. Despite the outstanding materials properties and device performances of hybrid perovskites, there are constraints that need to be resolved in order to attain full optoelectronic applications and commercialization. Some of these challenges include enhanced device efficiency, long-term stability and toxicity.

The rapid research progress and great strides been made by metal halide perovskites in optoelectronics call for swift and consistent survey into the state of the field. There have been recent excellent review papers spanning from bulk crystals to nanocrystals which covers fundamental physical properties and devices [49–53]. Each of these corresponding reviews has a different line of narrative, focus, and depth. For instance, Rogach and coworkers summarized the developments on perovskite NCs from synthesis to their applications [52]. However, reviews focused on perovskite (both bulk and nanocrystals) light emitting applications are limited [51]. This paper therefore covers recent achievements, ongoing progress and the challenges of perovskites from the perspective of both materials and devices with an emphasis on light emission. We begin by offering recent research activities that have been geared towards the broadening of the light absorption/emission spectral range of metal halide perovskites and the narrowing of their emission peaks. The subsequent section comprehensively reviews the photophysical characteristics of these materials. We particularly address their optical properties related to the requirements for solid state light emitting applications. Their exploitation in light emitting diodes and diode lasers is also highlighted. The last section explores the current challenges for light emitting applications of perovskites and presents our perspectives on these applications.

Metal halide perovskites for light emission

Tunable light emission and high color purity perovskites

Color (bandgap) tunability is one of the exceptional characteristics of hybrid perovskites compared to other non-molecular semiconductors. The color tunability or bandgap engineering in this class of materials is achieved through tailoring of the chemical composition, nanostructuring and quantum confinement. A considerable number of reports have demonstrated that the emission wavelengths are tunable from the ultraviolet to the near-infrared spectral regions (390–1050 nm) [25,32,34,54–57].

Tunable band-gap by composition

Long before 3D halide perovskites were employed in solar cells, Kitazawa *et al.* [58] studied the optical properties of methylammonium lead trihalides [CH_3NH_3(=MA)PbX_3 (X = Cl, Br, I)] and their mixed-halide crystals and showed that by varying the halide composition, the bandgap can be tuned to obtain 1.55 eV (X = I), 2.23 eV (X = Br) and 3.11 eV (X = Cl). The bandgap of the mixed-halides yielded values that range between the values of the pure halide perovskites. Notably, the pioneering works on perovskite solar cells were based on thin films of pure halide perovskites, $MAPbI_3$ and $MAPbBr_3$ with absorption onsets at ~800 nm and ~570 nm respectively [28]. Snaith and co-workers later chemically modified the $MAPbI_3$ by partial substitution of the iodide with chloride ions which resulted in a small blue-shift in the absorption onset, better stability, and enhanced carrier transport than the pure halide perovskites [30]. In order to enhance the perovskite light harvesting capabilities, Noh *et al.* [59] made $MAPb(I_{1-x}Br_x)_3$ $[0 \leq x \leq 1]$ perovskites by stoichiometric mixing of the iodides and bromides and demonstrated that the bandgap of the perovskite thin films can be chemically tuned by controlling the ratio of the halides. Thus, they showed that this class of materials could absorb in almost the entire visible spectrum. Their findings stimulated bandgap engineering of perovskite materials for wider spectrum emission and enhanced light emission applications.

By controlling the halide ratio of $MAPbX_3$ (X = Cl, Br, I) perovskite films, Xing and colleagues [20] demonstrated continuously tunable amplified spontaneous emission (ASE) and lasing at wavelengths between ~390 and 790 nm. Subsequently, using methylammonium-based perovskites, Tan *et al.* [27] fabricated halide perovskite LED (PeLED) that yielded bright (luminance of 364 cd m^{-2} at current density of 123 mA cm^{-2}) visible and infrared electroluminescence. Also, by employing $MAPbBr_3$, $MAPbBr_2I$ and $MAPbI_{3-x}Cl_x$, they observed electroluminescence at 517 nm (bright green), 663 nm (red) and 773 nm (near-infrared), respectively. These earlier works have paved the way for an influx of perovskites with broadly tuned band gaps. Thus, several other reports have demonstrated color tunability through halide substitution and mixing using different synthetic methods and starting precursor sources. For example, Sadhanala *et al.* [23] demonstrated blue-green (~3.1–2.3 eV (425–570 nm)) color tunability in $MAPb(Br_xCl_{1-x})_3$ $[0 \leq x \leq 1]$ perovskites using lead acetate instead of the commonly used lead halides as the lead precursor source.

Although halide mixing has expanded the choices of perovskites for broad emission, mixed-halide perovskites are faced with the daunting challenge of light-induced instability, which poses itself as a bottleneck to the effective operation and reliability of

optoelectronic devices. This instability arises from halide migration under continuous light illumination, which results in phase segregation and formation of traps or domains of the corresponding pure halides. Even though the phenomenon is reversible as demonstrated by McGehee and coworkers [60], the ultimate long-term use of mixed-halide perovskites in optoelectronics requires a solution to this challenge as proposed by Slotcavage et al. [61].

Color tuning through cationic substitution and mixing have also been reported. The common cations employed are methylammonium (MA), formamidinium (FA) and cesium (Cs) for the A position and lead (Pb) and tin (Sn) for the B position. Bandgap tuning of perovskites by cation substitution was first demonstrated in photovoltaic devices by Snaith and colleagues where they found that, replacing the MA cation (2.70 Å) in $MAPbI_3$ perovskite with Cs^+ ion (1.81 Å), which is smaller in size increases the bandgap from 1.55 eV to 1.73 eV, while the replacement with the slightly larger FA cation decreases the bandgap from 1.55 eV to 1.48 eV [32]. Although the change in wavelength range is small compared to that determined by the anionic substitution, their result showed that as the A-cation increases in size, the bandgap decreases, leading to a red-shift in the absorption onset.

To understand the interplay between cationic size and the electronic properties, Amat *et al.* [62] investigated the effect of A-cation size on $APbI_3$ perovskites with A = Cs^+, MA and FA using first-principles calculations. They confirmed the experimental observation that increasing the cation size leads to redshift in the absorption onset of the material. They also observed that the hydrogen bonding between the cation and the inorganic octahedral network is enhanced, resulting in the modification of the ionic/covalent character of the Pb–I bonds. Although bond modification plays a role in the shift of the absorption onset, it is not the primary cause. Prior to this study, several other investigations geared towards unraveling the role of ionic size and orbital contributions to the electronic properties of these materials have been performed on typical halide perovskites using ultraviolet photoelectron spectroscopy studies and first-principles calculations. For instance, in $MAPbI_3$, it was found that the valence band maximum (VBM) consisted of Pb 6s–I 5p sigma-antibonding orbitals while the conduction band minimum (CBM) consisted of Pb 6p–I 5s and Pb 6p–I 5p pi-antibonding orbitals [63]. Similar studies on tin-based perovskites revealed that the same phenomenon is observed involving tin (Sn) and the halide orbitals. In addition, investigation by Borriello *et al.* [64] on tin halide perovskites showed that the size of the A-cation significantly influences structural stability and electronic properties of the perovskites. Their studies revealed that the bandgap which is determined from the VBM and the CBM consisted solely of orbital contributions from the inorganic octahedron $(BX_4)^{6-}$ and that the orbitals of the A-cation do not contribute to the energy bands. Furthermore, it was found that structural parameters such as in-plane B–X–B bond angle and B–X bond length which are significantly modified by the A-cation are primarily responsible for the observed changes in the electronic and optical properties of the materials [63,65–73]. This understanding prompted A-cation mixing in perovskites with the aim of not only enhancing structural stability but also tuning the absorption/emission wavelengths. Most researchers have therefore as a design principle turned their research attention to cation combination of the most commonly studied A-cations (Cs^+, MA and FA), forming double [74] or triple [75] cation-blended perovskites. Similarly, Hao *et al.* [57] have exploited the bandgap behavior of mixed B-cation $MA(Sn_{1-x}Pb_x)I_3$ $[0 \leq x \leq 1]$ perovskites and found an anomalous bandgap tuning behavior that deviated from the usual linear trend observed in for example mixed halide perovskites where the bandgap lies between the two extremes of either of the pure materials. Far from the expected bandgap tuning between 1.55 eV for the 100% lead sample ($MAPbI_3$) and 1.35 eV for the 100% tin sample ($MASnI_3$), they observed bandgap as narrow as 1.1 eV for equal mole ratios of Pb/Sn, therefore pushing the absorption onset into the near-infrared (~1050 nm).

Besides 3D hybrid perovskites, tunable light emission in two-dimensional (2D) layered perovskites has also been demonstrated. For example, by replacing MA in 3D $MAPbI_3$ with different phenylalkylammonium cations, Kamminga *et al.* [76] successfully synthesized layered hybrid structures, showing that by increasing the alkyl chain lengths, the bandgap could systematically be increased from 2.12 to 2.48 eV. Sargent and coworkers have also shown that increasing the number of the inorganic monolayer sheets, that is, forming multilayered quasi-2D perovskite structures, significantly red-shifts the PL peak [77]. A similar observation was recently reported by Huang and coworkers in $NFPI_7$ multiple quantum wells (made from precursor solution of 1-naphthylmethylamine iodide (NMAI), FAI and PbI_2) [78].

Tunable band-gap by nanocrystal shape and size

Beyond bulk perovskite crystals, broad color tunability has also been reported in perovskite nanocrystals. Bandgap engineering and color tuning in perovskite nanocrystals is achievable through nanostructuring (i.e. size and shape). The nanostructures that have been reported include nanoparticles (NPs) [79–81], nanowires (NWs) [82] and nanoplatelets (NPLs) [83,84]. Similar to bulk perovskite crystals, color tuning in perovskite nanostructures by compositional control has been demonstrated. For example, colloidal nanocrystals of mixed-halide (octylammonium (OA):MA)PbX_3 (X = Cl, Br, I and mixture thereof) of size ~5–10 nm, were demonstrated by Pathak *et al.* [25] to show a continuously tunable PL emission from 385 to 770 nm by varying the halide composition. The formation of nanoplatelets having excess amount (>60%) of OA in the A-cation mixture was also demonstrated. Figure 2a shows images of representative perovskite nanocrystals of (OA:MA)PbX_3 with X = Cl, Br and I, stabilized in polystyrene with emissions in blue, green and red respectively. Interestingly, the first composition-tunable colloidal $MAPbX_3$ (X = Cl, Br, I or mixture thereof) perovskite nanocrystals were fabricated using ligand-assisted reprecipitation (LARP) technique. The nanocrystals yielded emissions in the wavelength range of 400–750 nm via the variation of the halide components [81]. The composition-tunability was further demonstrated by embedding $MAPbX_3$ nanocrystals (size ~3–5 nm) in polyvinylidene fluoride (PVDF) composites films with the aim of enhancing luminescence and materials stability besides color tuning [85]. Kovalenko and co-workers also demonstrated successful synthesis, color tuning and size control in fully inorganic $CsPbX_3$ nanoparticles, with emissions from 410 to 700 nm [40]. This was achieved through controlled synthesis of monodisperse nanocubes with crystal sizes tunable between 4 and 15 nm by controlling the reaction temperature between 140 and 200°C. The

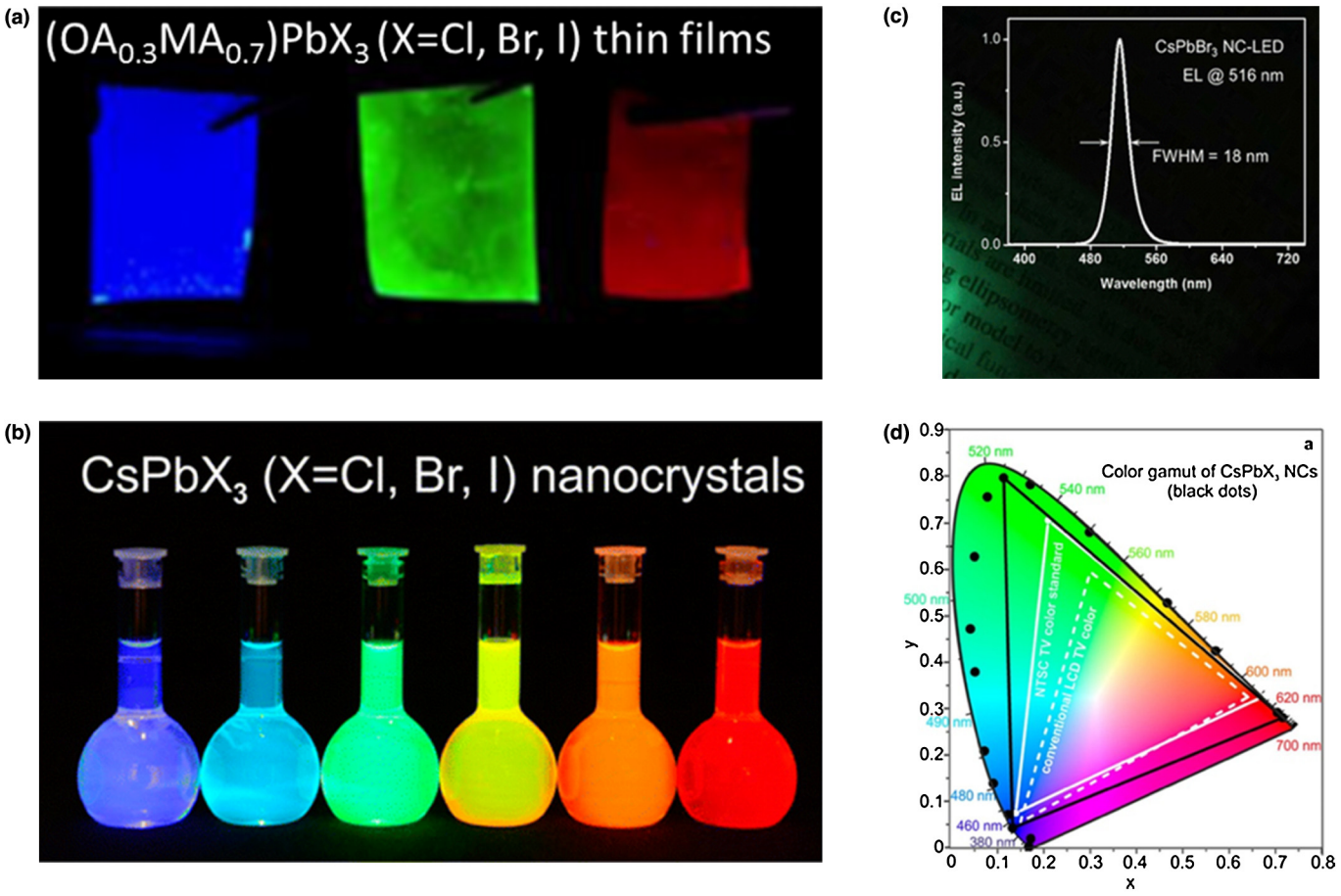

FIGURE 2

(a) Pictures of perovskite crystal/polymer composite films emitting blue (X = Cl), green (X = Br) and red (X = I) light under a UV lamp (365 nm). Reprinted with permission from [25]. Copyright 2015, American Chemical Society. (b) Pictures of flasks containing solution of color tunable colloidal $CsPbX_3$ nanocrystals [40]. (c) Normalized EL spectra of $CsPbBr_3$ NC-LED with emission peak centered at 516 nm [40]. (d) Representative CIE diagram showing the coordinates of $CsPbX_3$ NCs. Reprinted with permission from [40].

pictures of flasks containing color tunable colloidal $CsPbX_3$ nanocrystals are shown in Fig. 2b.

Pure color emission perovskites

Color purity is a key property for display applications. The use of the CIE chromaticity diagram (introduced by the Commission Internationale de l'Eclairage) allows the objective specification of color quality by mapping colors visible to the human eye in terms of hue and saturation. Similarly, the spectral purity of light emission is often specified by full-width at half-maximum (FWHM) with narrow bandwidths indicative of high color purity. In the past two years, several reports have demonstrated PL and EL emissions in single crystals, thin films and nanocrystals of hybrid perovskites with ultra-high color purity which are evident by their narrow bandwidths (~20 nm or less) and pure hue [23,86]. A notable example is the bright-green EL emission displayed by $CsPbBr_3$ NC-LEDs centered at 516 nm with FWHM of 84 meV (18 nm) and CIE color coordinates of (0.09,0.76) (Fig. 2c) [86]. Friend and co-workers [23] also showed that besides exceptional bandgap tuning, the color purity of $MAPb(Br_xCl_{1-x})_3$ $[0 \leq x \leq 1]$ perovskite LEDs (PeLEDs) can be refined by varying the halide ratio. They demonstrated blue-green LEDs based on $MAPb(Br_xCl_{1-x})_3$ perovskites with FWHM as narrow as 34 meV (5 nm for 100% chloride content) which depends on the ratio of the halide composition. Furthermore, as a representation of the wide and pure color gamut provided by metal halide perovskites, Fig. 2d shows the emission of the $CsPbX_3$ NCs reported as black dots on the CIE chromaticity diagram. The color coordinates lie along the spectral locus of the color gamut with each point representing a pure hue of monochromatic light or pure color. The diagram also illustrates the comparison of the color triangle of perovskites to other most common color standards used in conventional LCD TV and the one of the NTSC TV (National Television System Committee), with the perovskites encompassing more than 100% of the NTSC standard [40,87].

Charge-carrier recombination and PLQY in hybrid perovskite

The most important figure of merit for high performance light-emitting materials is the photoluminescence quantum yield (PLQY) which is defined as the number of photons emitted per absorbed photons of the excitation source. Photoluminescence emission in materials is due to radiative recombination processes, which directly compete with non-radiative processes that are either intrinsic or extrinsic (as a result of traps or defects). Charge-carrier recombination processes involved in hybrid perovskites are monomolecular recombination, bimolecular recombination

and Auger recombination. Assuming that both monomolecular recombination and Auger recombination are purely nonradiative and only bimolecular recombination is radiative, the PLQY, also referred to as radiative efficiency is then given by the ratio of radiative to total recombination rates and stated mathematically as below.

$$\emptyset(n) = \frac{nk_2}{k_1 + nk_2 + n^2k_3}$$

where n is the charge-carrier density, k_1, k_2 and k_3 are the monomolecular, bimolecular and Auger recombination rate constants, respectively [88]. Experimental evidence showed that at low excitation fluence, the carrier recombination is dominated by trap-mediated (monomolecular) recombination (known as Shockley–Read–Hall recombination in the solar cell community) while the bimolecular and Auger recombination only appears at high fluences [89].

In their earlier study in 2014 of the optical properties of solution-processed $MAPbI_{3-x}Cl_x$ perovskite thin films, Friend and collaborators [45] showed that the PL with a relatively narrow band centered around 1.6 eV exhibited a relatively low PLQY at low fluences (<25 mW/cm^2) which rapidly increased with increased excitation densities to a maximum value of 70%. They attributed the rapid increase in PLQY to dominant radiative recombination at the high fluences. This claim is evidenced in $MAPbI_3$ and $MAPbI_{3-x}Cl_x$ as shown in Fig. 3a. The figure illustrates the dependence of time-integrated PL signals and QY on injected

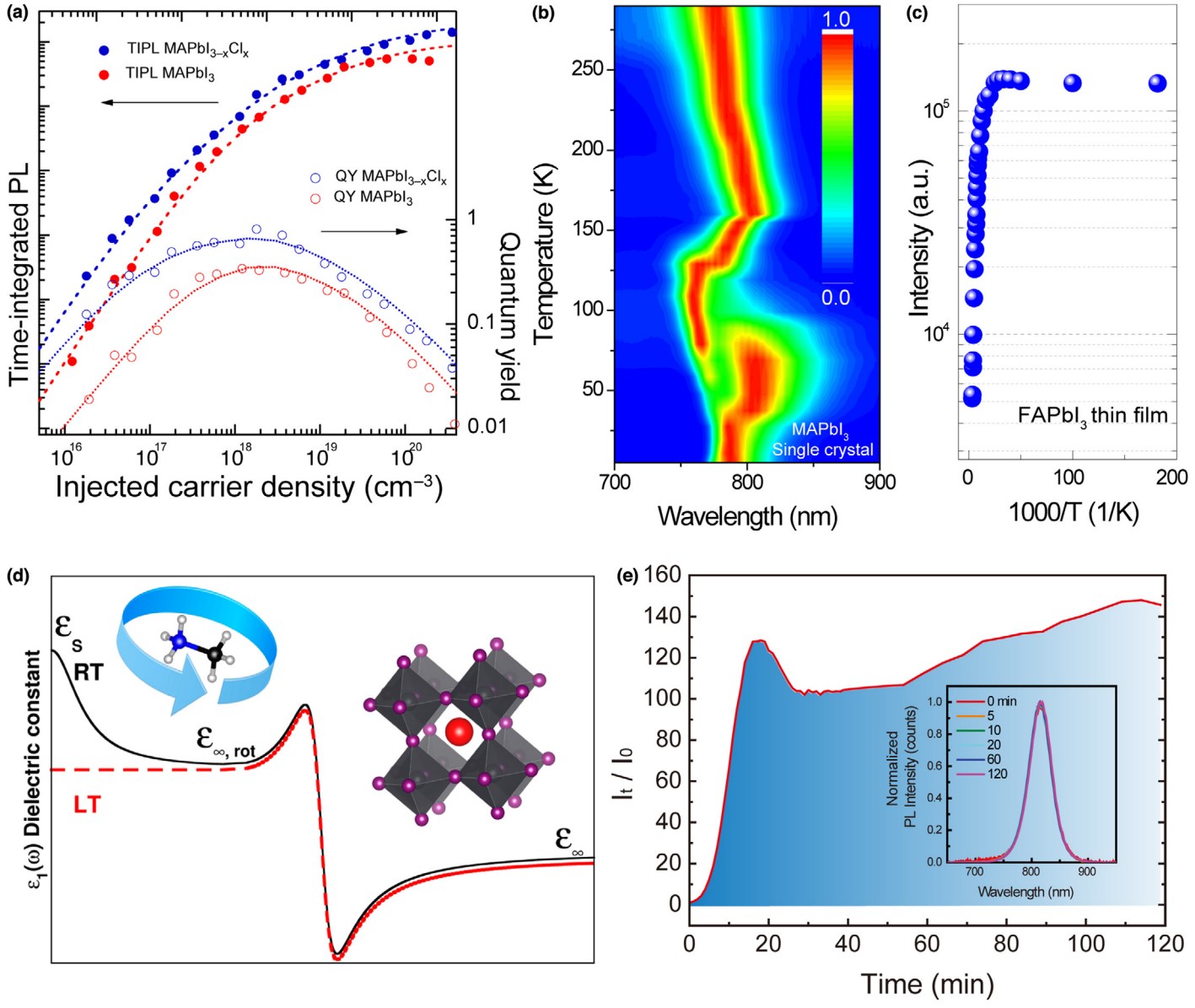

FIGURE 3

(a) Time-integrated photoluminescence signals and quantum yield as a function of injected carrier density for the two perovskite samples. Reprinted with permission from [89]. (b) 2D pseudo-color plot of the normalized emission spectra from $MAPbI_3$ single crystal at different temperatures. Reprinted with permission from [90]. (c) Integrated PL intensity as a function of temperature in $FAPbI_3$ thin film. Reprinted with permission from [91]. (d) Schematic drawing of the dielectric constant as a function of frequency for the low and room temperature phases. Reprinted with permission from [142]. (e) Dynamics of the photoluminescence intensity under illumination of laser in air. Reprinted with permission from [101].

carrier density. Thus, given that at low excitation fluence the carrier recombination is dominated by monomolecular recombination, the linear growth in QY is attributed to increased bimolecular radiative recombination, while the saturation and eventual drop at very high carrier densities is attributed to Auger processes. This deduction is based on the scaling of the various recombination terms in the radiative efficiency relation dependence on the injected charge density.

As mentioned above, the photoexcitations in bulk hybrid perovskites (for example, $MAPbI_3$ crystals [90]) have been demonstrated to lead to mostly free carriers at room temperature. This is because of exciton screening by collective orientational motion of the organic cations, leading to low exciton binding energy at room temperature (Fig. 3b–d). The radiative recombination is thus mainly dominated by bimolecular recombination at room temperature while Wannier-like excitons are evidenced at low temperature [91]. This nature of the radiative recombination leads to relatively low photoluminescence intensity at low excitation fluence at room temperature but significantly increases with decreasing temperature. As shown in Fig. 3c, the PL intensity in formamidinium lead iodide ($FAPbI_3$) thin film at 5 K is about 25 times greater than that at 295 K. Therefore, trap-assisted recombination, which is highly dependent on materials quality (trap density) need to be well addressed for devices operated at low carrier density. It has been shown that the trap density in perovskite thin films varies from 10^{14} to 10^{17} cm^{-3} [92–94] resulting in a wide range of charge-carrier lifetimes. On the other hand, in single crystals, much lower trap densities (10^9–10^{10} cm^{-3}) are observed [38]. Recent theoretical studies on both iodide- and bromide-based perovskites revealed that the defects in these materials have low formation energies that create only shallow levels [95–97], and that these traps can be passivated effectively [98,99]. Noel *et al.* [78] used Lewis bases thiophene and pyridine to passivate the perovskite and demonstrated an enhanced PL lifetime in the order of 2 μs. Furthermore, Zhang *et al.* [93] showed that the addition of hypophosphorous acid (HPA) in the precursor solution significantly improved the film quality, both electronically and topologically. Similar improvement in film quality and surface passivation was recently demonstrated using amine functional molecules, leading to enhancement in photovoltaic performance and air-stability [100]. Also, laser treatment in controlled environment has been demonstrated as a way of suppressing trap states. Such 'Light curing' effects in perovskites have been experimentally observed independently by Fang *et al.* and deQuilettes *et al.* [101,102] and theoretically demonstrated in $MAPbI_3$ by Filippo De Angelis and coworkers [103]. As shown in Fig. 3e, the photoluminescence intensity is enhanced more than 140 times after continuous ultraviolet laser illumination [101]. Very recently, we also demonstrated that the surface trap state in methylammonium-lead tribromide ($MAPbBr_3$) single crystals can be reduced to 10^8 cm^{-2} upon exposure to oxygen and water vapor, leading to an unusually low surface recombination velocity (SRV) of 4 cm/s, and extremely long photoluminescence lifetime above 4 μs (Fig. 4) [104].

To overcome the limitation of the bimolecular recombination and ensure enhanced PL at low excitation, one of the strategies adopted was the formation of nanostructures with reduced dimensionalities for quantum confinement. This leads to a transition

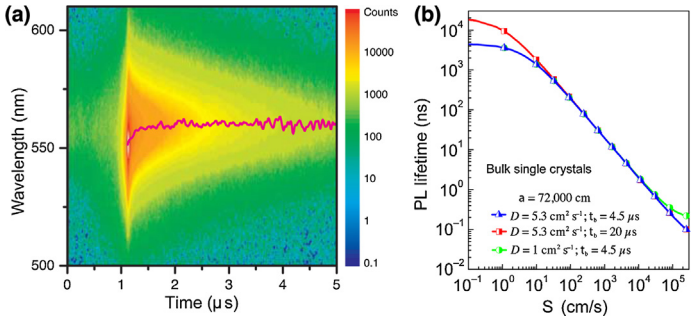

FIGURE 4

(a) Two-dimensional (2D) pseudocolor plots of TRPL spectra of a $MAPbBr_3$ single crystal taken in air. (b) PL lifetime in $MAPbBr_3$ single crystals as a function of surface recombination velocity for various carrier diffusion coefficients and bulk lifetimes. Reprinted with permission from [104].

from continuous to discrete energy levels with the energy gap inversely proportional to the particle size. Compared to the bulk halide perovskites, perovskite nanocrystals have been shown to exhibit higher PLQY due to quantum confinement effect, which promotes efficient radiative recombination. For example, colloidal $MAPbX_3$ NPs (X = Cl, Br, I) fabricated using ligand-assisted reprecipitation (LARP) method have been shown to exhibit PLQY in the range of 50–70% at room temperature at low excitation fluences [81]. The PLQY of the NPs were found to be size-dependent, with the smallest $MAPbBr_3$ NP (≈3.3 nm) yielding the highest PLQY. Modification of the above technique with increased $MABr/PbBr_2$ ratio also led to an enhanced PLQY of about 83%. Furthermore, by fine-tuning the LARP technique, $MAPbBr_3$ NPs synthesized at different temperatures of 0–60°C have been demonstrated to exhibit size-tunable bandgap (475–520 nm) for particle sizes in the range of 1.8 – 3.6 nm and exceptional PLQY values of 84–93% respectively [79]. The FWHM of the emission bands are in the range of 128–198 meV with short radiative lifetimes of 13–27 ns compared to the bulk materials that have lifetimes of the order of 100 ns. Similarly, Huang *et al.* [105] employed emulsion synthesis method to synthesize $MAPbBr_3$ NPs with the use of controlled amounts of demulsifier to tune the nanoparticle size in the range of 2–8 nm which yielded PLQY between 80 and 92%. Although the size-dependent PLQY is not very obvious for particles larger than 2.6 nm due to weak confinement effect, the highest PLQY was obtained for the smallest NP. Additionally, it was illustrated recently that by embedding nanocrystals of sizes ~3–5 nm in a PVDF composite film, the PLQY is enhanced to 95% [85]. Besides high PLQY in the hybrid perovskite nanocrystals, Kovalenko and coworkers have also demonstrated nanoparticle size-dependent PLQY values in the range of 50–90% in inorganic perovskite $CsPbX_3$ NPs (4–15 nm) prepared using the hot-injection technique at temperatures of 140–200°C [40]. The nanoparticles also exhibited narrow emissions (88–106 meV) [40]. It is important to underline that in nanoparticles, the PLQY is enhanced not only because of the confinement but also because of the surface passivation. For example, using an inorganic–organic hybrid ion pair such as didodecyl dimethylammonium sulfide (S^{2-}–DDA^+) to passivate surface defects in perovskite $CsPbBr_3$ quantum dots, the radiative recombination is enhanced, resulting in an increase in PLQY from 49% to 70% [106]. The devices also exhibited air- and photo-stability.

It is worth noting that beyond nanoparticles, high PLQY values have been demonstrated in other nanostructures such as nanowires, nanoplatelets and nanorods [40,43,84,107,108]. Additionally, multilayered multiphased quasi-2D dimensional perovskite solids [$PEA_2(MA)_{n-1}Pb_nI_{3n+1}$, where PEA = $C_8H_9NH_3$ and n = number of layers] have been employed to confine charge carriers within the multicomponent emissive layer. In this way, the perovskite emissive layer also serves as charge carrier concentrator, guiding the charge carriers to the smaller bandgap emitting regions and enabling efficient radiative recombination even at relatively low fluences. This leads to efficient PeLED with EQE of 8.8% and radiance of 80 W sr^{-1} m^{-2} [77].

For laser applications where the device operates under high charge carrier density (>10^{18} cm^{-3}), Auger recombination competes with radiative recombination, hence ought to be taken into consideration. Saba *et al.* [89] showed that the maximum PL quantum yield in $MAPbI_3$ and $MAPbI_{3-x}Cl_x$ is achieved for carrier density range of $n_0 = 0.5–3 \times 10^{18}$ cm^{-3} and that non-radiative Auger processes dominated at higher excitations (>10^{19} cm^{-3}). This is an important condition for potential lasing applications, where rapid Auger processes compete with population inversion. Depending on the electronic properties, the Auger-recombination rate constants in perovskite films have been shown to vary in the range $0.99–13.5 \times 10^{-28}$ cm^6 s^{-1} [109–111]. These values are of the same order of magnitude as for bulk PbSe ($C \approx 8 \times 10^{-28}$ cm^6 s^{-1}) [112]. Interestingly, it has been shown by Zhu *et al.* [43] that the Auger recombination in $MAPbI_3$ nanowires is negligible at the lasing threshold. It is competitive only when the carrier density is 10^3 times higher than the lasing threshold. These features make organometallic perovskites very promising for the realization of a solution-processed electrically driven laser.

Applications: LED and lasing

Perovskite light-emitting diodes (PeLEDs)

The demonstration of electroluminescence in halide perovskites was first observed in layered perovskites at cryogenic temperatures in the early 1990s [113–115] and later at room-temperature by incorporating a specially modified quaterthiophene dye in the hybrid perovskite sheet [116]. Although research activities in this field were inactive for over a decade, recent interest has been rekindled by the interesting photoluminescence properties observed in solution-processed 3D perovskites.

The device architecture of PeLED can be classified into multi-layered and single-layered device structures. A typical multi-layered PeLED device consists of a front transparent electrode (typically FTO or ITO), an n-type hole-blocking layer (HBL), a p-type electron-blocking layer (EBL), a perovskite emitter and a back electrode. The perovskite active layer is sandwiched between the HBL and the EBL to form a double-heterojunction structure in order to confine the injected charges for better light emission. Under applied voltage, the electrodes inject charge carriers through the transporting layers into the perovskite active layer where they recombine radiatively, emitting light. In general, multi-layered PeLEDs have two main device geometries: the conventional (HBL/perovskite/EBL) and inverted (EBL/perovskite/HBL) configurations. These configurations are adapted from the basic device structures employed in solar cells. The typical schematic diagrams of the device geometries (conventional and inverted) and some of the reported carrier blocking layers are shown in Fig. 5a–c. Alternatively, the single-layered PeLED device is composed of a perovskite composite sandwiched between an anode and a cathode. The most commonly used perovskite emitters are based on $MAPbX_3$ and $CsPbX_3$ (X = Cl, Br, I or a mixture thereof) family of halide perovskites, although recent reports also demonstrated the use of mixed-cation PeLEDs [117].

The first single-layered PeLED consisted of a composite of $MAPbX_3$ (X = Cl, Br, I) and poly(ethylene oxide) (PEO) sandwiched between indium-doped tin oxide (ITO) as the anode and In/Ga or Au as cathode. The best performing device which is based on PEO:$MAPbBr_3$ (0.75:1 weight ratio) displayed green emission with maximum luminance of 4064 cd m^{-2} at 5.5 V, comparable to earlier results of the multi-layered devices [118]. By replacing the emissive layer with a mixture of $CsPbBr_3$, PEO and poly(vinylpyrrolidone) (PVP), the device performance has been significantly enhanced, yielding green luminescence with luminance of 591,197 cd m^{-2} at 4.8 V and EQE of 5.7% [119].

Similarly, the first reported multi-layered 3D perovskite LEDs displayed near-infrared, green and red emissions by employing $MAPbI_{3-x}Cl_x$, $MAPbBr_3$ and $MAPbBr_2I$ as the emitting layers. The optical absorption, photoluminescence and electroluminescence spectra of these early devices are illustrated in Fig. 5d [27]. Due to the different energy levels of the perovskite emitters and for the purposes of effective charge injection and confinement, the $MAPbI_{3-x}Cl_x$ was sandwiched between titanium dioxide (TiO_2) and poly(9,9-dioctylfluorene) (F8) layers which functioned as HBL and EBL respectively while in the case of the green and red emissions, the perovskite emitters were sandwiched between PEDOT:PSS and F8 which functioned as EBL and HBL respectively. With these configurations, external quantum efficiency (EQE) of 0.1% and maximum luminance of 364 cd m^{-2} for the green-emitting devices, were reported. About the same time, Kim *et al.* [120] also reported a green-emitting PeLED with slightly improved EQE of 0.125% and luminance of 417 cd m^{-2} by sandwiching the perovskite $MAPbBr_3$ between a self-organized buffer hole-injection layer (Buf-HIL) that is composed of PEDOT:PSS and a perfluorinated polymeric acid, tetrafluor-oethylene-perfluoro-3,6-dioxa-4-methyl-7-octene-sulfonic acid copolymer (PFI) and the hole-blocking material, 2,2′,2″-(1,3,5-benzinetriyl)-tris(1-phenyl-1-H-benzimidazole) (TPBI). These earlier works paved the way for further exploration of this class of materials for enhanced PeLEDs. Through the enhancement of perovskite processing and/or film formation, materials and interface engineering, use of various interfacial layers with tailored band alignments and the selection of appropriate electrodes, the PeLEDs device performances have been greatly enhanced over the past two years. For example, the formation of metallic lead (Pb) in $MAPbBr_3$ that has been shown to limit the electroluminescence efficiency through exciton quenching has been reduced through the modification of the perovskite composition by slightly increasing the MABr molar proportion in the $PbBr_2$/MABr mixture [22]. In addition, $MAPbBr_3$ nanograins have been created to confine the excitons, leading to enhanced luminescence with current efficiency and EQE of 42.9 cd A^{-1} and 8.53% respectively [22]. More recently, PeLEDs based on solution-processed self-organized multiple quantum wells have been demonstrated to exhibit a record EQE of 11.7% at a current density of 100 mA cm^{-2} [78]. Although these values are below the record

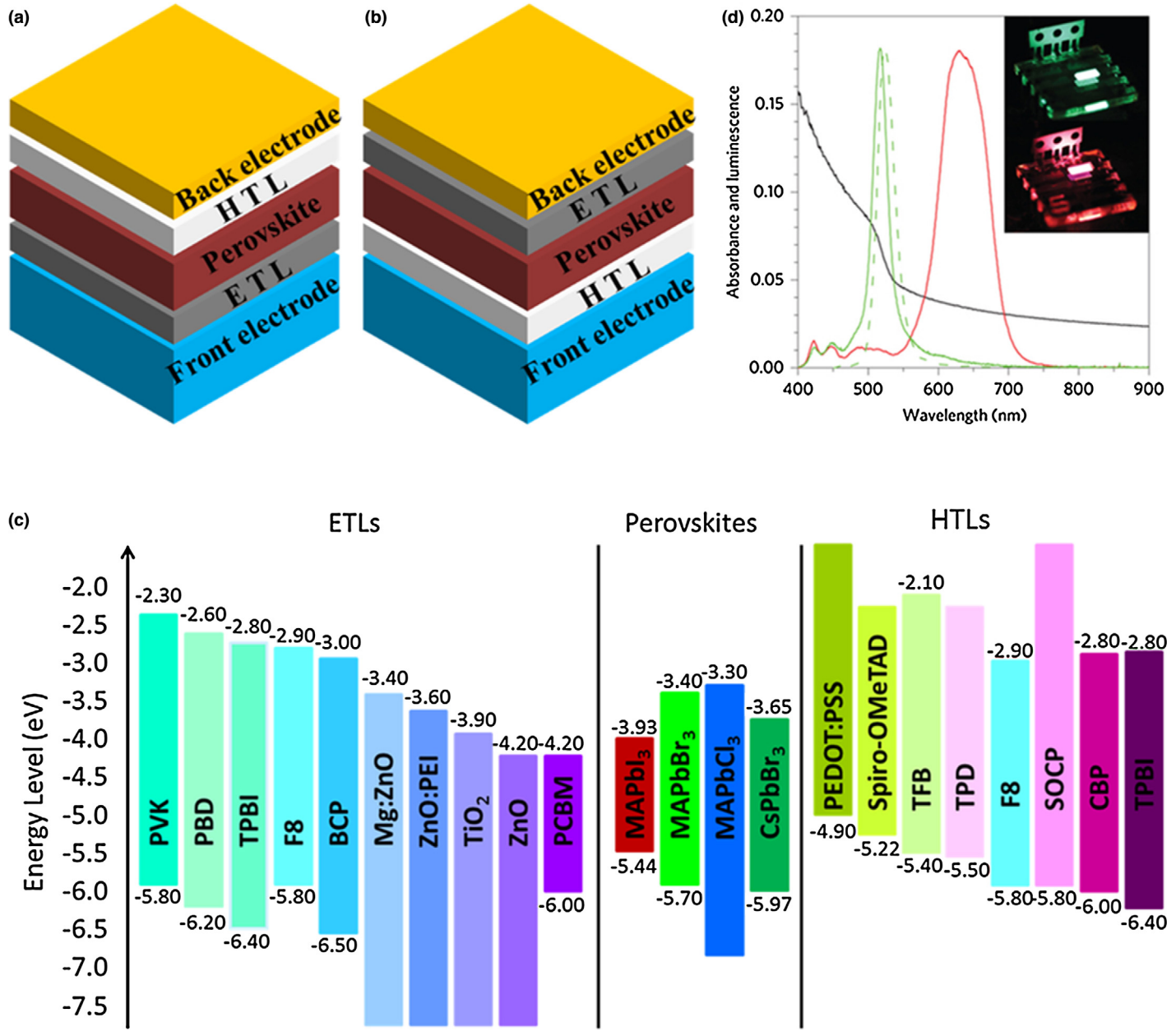

FIGURE 5

(a,b) Schematic diagrams of the PeLED architectures in the conventional and inverted configuration respectively. (c) Energy level alignment of various materials used as perovskites, ETLs and HTLs in the PeLEDs that have been reported. (d) Optical absorption is shown with the black line. Normalized electroluminescence and photoluminescence spectra of $MAPbBr_3$ perovskite are shown in solid and dashed green lines respectively. The red line is the normalized electroluminescence spectrum of $MAPbBr_2I$ mixed halide perovskite. Inset image: uniform green and red electroluminescence from $MAPbBr_3$ and $MAPbBr_2I$ PeLEDs, respectively. Reproduced with permission [27]. Copyright 2014, Nature Publishing Group.

values of solution-processed Organic LEDs (OLEDs) and Quantum Dots LEDs (QLEDs) (EQE > 20%), PeLEDs show high promise as the future of solid-state light emitting applications. Besides red and green emissions, blue emission [23] has also been demonstrated, leading to the first demonstration of perovskite white-light LED by Snaith and co-workers [25], which was achieved by blending perovskite nanocrystals with different emission wavelengths in a polymer host. Using mixtures of multiple color-emitting $CsPbX_3$ nanocrystal powders, down conversion white light-emitting devices were demonstrated [121]. The $CsPbX_3$ nanocrystals were coated with water resistant polyhedral oligomeric silsesquioxane (POSS), which prevents anion exchange between perovskite nanocrystals of different compositions and preserve their distinct emission spectra. In addition to PeLEDs, electroluminescence has also been demonstrated in field-effect transistors (FETs) at low temperatures (<200 K). Using bottom-gate bottom-contact configuration with heavily p-doped Si as the gate contact and Au as the source-drain contact, Soci and coworkers demonstrated ambipolar charge injection and gate-dependent electroluminescence in $MAPbI_3$-based FETs. The emitted light was only observed in the ambipolar regime at low temperatures (78–178 K). The authors also found that the charge mobility increased by 2 orders of

magnitude when the temperature was lowered from room temperature to 78 K [48], a characteristic that is consistent with phonon scattering-limited transport of conventional inorganic semiconductors.

Perovskite halides for lasing

Observation of amplified spontaneous emission (ASE) is a direct criterion for identifying intrinsic gain properties of laser materials. Room temperature ASE was first reported in $MAPbI_3$ thin films [20], with a threshold carrier density of $\sim 1.7 \times 10^{18}\ cm^{-3}$. The threshold is comparable with state-of-the-art cavity-free solution-processed polymer films such as poly[9,9-dioctylfluorene-co-9,9-di(4-methoxyphenyl)-fluorene] (F8DP). Notably, Deschler *et al.* [45] constructed and demonstrated the operation of an optically pumped vertical cavity laser comprising a layer of perovskite between a dielectric mirror and evaporated gold top mirrors. The photoexcitation of $MAPbI_{3-x}Cl_x$ mixed-halide perovskite results in free charge carrier formation within 1 ps and these free charge carriers undergo bimolecular recombination on time scales of tens to hundreds of ns. Through variable stripe length measurements, a net peak gain value of $125 \pm 22\ cm^{-1}$ and a gain bandwidth of 50 ± 14 meV has been determined in $MAPbI_3$ thin films [122]. Sargent and coworkers also showed that the optical gain can be as high as $3200 \pm 830\ cm^{-1}$ [123]. In $CsPbX_3$ perovskite nanocrystals, values of gain from 450 to $500\ cm^{-1}$ were reported [124]. Values of this magnitude are comparable to those obtained in colloidal quantum wells ($600\ cm^{-1}$) [125] and higher than some polymer gain values (for example, net gain of $18\ cm^{-1}$ was reported in conjugated polymer) [126]. In addition, gain in perovskite thin film has been shown to last as long as 200 ps. These superior properties make perovskite materials ideally suited for lasing operation.

As mentioned, hybrid perovskite thin films are processable either from solution or by evaporation, which enable microstructuring to impose an optical resonator as shown in Fig. 6a–d. Very recently, vertical cavity surface emitting (VCSEL) and photonic crystal (PhC) lasers have been demonstrated using perovskites. For example, Riede *et al.* [127] evaporated perovskite onto a nanoimprinted polymer resist to create a perovskite DFB cavity. The lasing wavelength was tuned between 770 and 793 nm simply by varying the grating periodicity. Giebink *et al.* [128] fabricated metal-clad $MAPbI_3$ distributed feedback lasers by a one-step spin coating process. The laser operated at a pump intensity threshold of $5\ kW/cm^2$ for durations of up to ~25 ns under InGaN diode laser excitation. Nurmikko *et al.* [129] also optimized the synthesis of the thin film to form a uniform distribution of perovskite nucleates, followed by thermal annealing to complete the crystal growth. With this synergistic materials and device approach, programmable, spatially patterned single mode lasing from a 2D pixelated perovskite photonic crystal (PePhC) laser array was realized.

Similarly, lasing from micro/nanocrystals of perovskites is also intensively investigated. Optically pumped lasers with micro/nano wire, microdisk, and microplatelet structure have been fabricated by chemical vapor deposition or solution growth methods. Cleanly

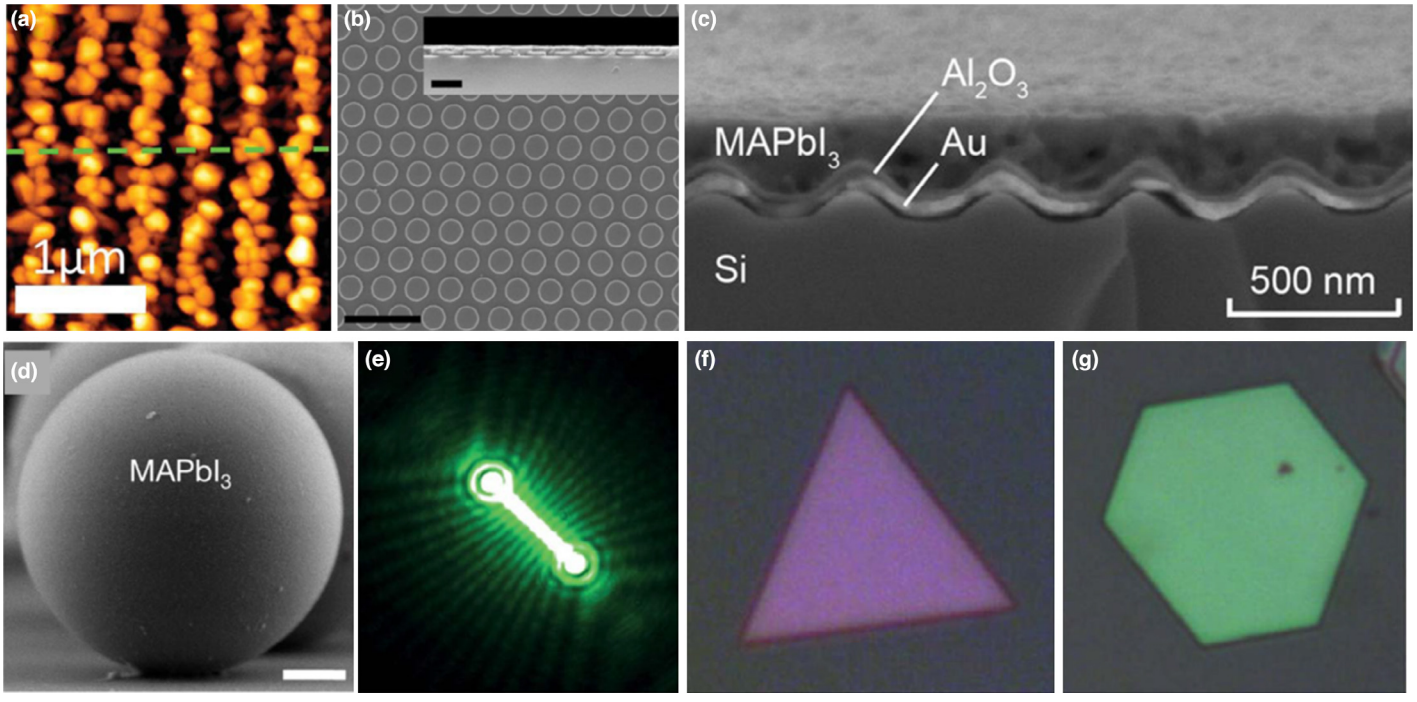

FIGURE 6

Perovskite laser device with varied optical resonators. (a) AFM image of a $MAPbI_{3-x}Cl_x$ perovskite distributed feedback (DFB) cavity [127]. (b) SEM image of photonic crystal optical resonator with $MAPbI_3$ perovskite film as active media. Reprinted with permission from [129]. Copyright 2016, American Chemical Society. (c) Scanning electron micrograph of a metal-clad, second order distributed feedback (DFB) $MAPbI_3$ perovskite laser constructed on a silicon substrate. Reprinted with permission from [43]. Copyright 2016, American Chemical Society. (d) Image of microsphere coated with $MAPbI_3$ perovskite. Reprinted with permission from [122]. Copyright 2014, American Chemical Society. (e) Fluorescence images of a single $MAPbBr_3$ NW above lasing threshold [143]. (f,g) Optical images of typical $MAPbI_3$ nanoplatelets under the illumination of white light. Reprinted with permission from [130]. Copyright 2014, American Chemical Society.

cleaved perovskite facets have also been obtained by making use of their well-defined crystalline structure to form a self-laser-cavity. These properties make perovskites attractive for potential applications as miniaturized solid-state lasers for sensing, quantum information processing, and on-chip photonics integration. Interestingly, single-crystal $MAPbX_3$ (X = Cl, Br, or I) nanowires with smooth end-facets have been fabricated with a surface-initiated solution growth strategy using a lead acetate ($PbAc_2$) solid thin film deposited on glass substrate and in contact with a high concentration of CH_3NH_3X in isopropanol [43]. Each of the NWs served as a waveguide along the axial direction and the two end-facets formed a high quality ($Q \sim 3600$) Fabry–Perot cavity for optical amplification. The reported lasing threshold (carrier density, 1.5×10^{16} cm^{-3}) is much lower than that of thin film counterparts, highlighting the versatility and prospects of perovskites for light-emission applications. By using chemical vapor deposition methods, Xiong *et al.* [130] successfully synthesized polygonal lead halide nanoplatelets, and then converted them into $MAPbI_{3-x}X_x$ (X = I, Br, Cl) perovskite nanoplatelets. The as-grown nanoplatelets showed well-defined triangular or hexagonal shapes with nanoscale thickness (10–300 nm) and edge length of several to tens of micrometer, able of forming whispering-gallery-mode (WGM) nanocavities. Notably, laser-diode arrays are essential light sources for sensing, displaying and other applications. Thus, patterned laser arrays and position-controlled growth are essential for integrated optoelectronic chips. In this regard, Liu *et al.* [131] recently demonstrated perovskite microplatelet arrays, which are fabricated on silicon with a pre-patterned single layer hexagonal boron nitride (h-BN) buffer layer. Interestingly, Feng *et al.* [43] developed a controllable dewetting technique for fabricating perovskite crystals by using a wettability-mediated micropillar-structured silicon template. Nucleation and growth of the perovskites were restricted in these microdomains, generating single-crystalline perovskite square microplate (SMP) arrays with precise positioning. This further expands the potential application of these perovskite microlasers in integrated photonic chips.

Conclusion and perspectives

Organic–inorganic hybrid perovskites have shown promising features for solid-state lighting and laser applications. PeLEDs with emissions across the visible to near-infrared and optically pumped lasers with low threshold have been achieved. However, as previously indicated, before these devices can approach commercialization, there are some challenges that need to be addressed.

Regarding perovskite light emitting diodes, the first thrust is to improve the device efficiency. As discussed above, the photoluminescence quantum yield (PLQY) of $MAPbX_3$ perovskite thin films are dependent on the excitation intensity and reaches higher values at high excitation photon fluences. In LED device applications, the injected carrier density is typically about $\sim 10^{11}$–10^{13} cm^{-3}, which is too low to fill the trap states completely. As a result, the actual PLQY under normal operating conditions is low. Thus, trap-mediated non-radiative recombination plays an important role in determining the device performance when operating under low carrier injection. Increasing the radiative recombination at low excitation is therefore critical for LED applications. Besides surface passivation of perovskite thin films, new strategies such as the recently developed technique to spatially confine the injected charges within perovskite nanograins are paramount [22]. As aforementioned, the reduced grain size aids in increasing the radiative recombination rate, which leads to an enhanced PLQY. One interesting strategy involves the synthesis of trap-free perovskite quantum dots, which will yield high efficient PeLED. However, it will require the balance of surface passivation and carrier injection using suitable ligands. Another aspect that has to be thoroughly addressed is to reduce leakage currents that demands perovskite thin films with better surface coverage. Rogach et al. demonstrated that the introduction of polyhedral oligomeric silsesquioxane to the solution increases the solubility of perovskite NCs and is a feasible way to form denser and thicker films [132].

Another challenge that requires much attention is the long-term material and device stability. As observed in the case of perovskite solar cells, the devices suffer degradation upon exposure to for example moisture, heat and light. This is related to both perovskite stability as well as the interfacial layers in the device. Since the degradation mechanisms are not fully understood in this materials and/or devices, further research is paramount to uncover the underlying mechanisms in order to devise means of mitigating the degradation processes and enhancing the long-term stability. In the case of moisture-induced degradation, one of the simplest approaches is to encapsulate the device. Alternatively, as already demonstrated by using water-resisting dodecyltrimethoxysilane, hydrophophic tertiary and quaternary alkylammonium [133,134] or fluorinated polymers [135] in solar cell devices, the perovskite LED stability can be improved by treating the surface with better multifunctional material coatings which are moisture-resisting and can withstand light and thermal stress [136]. For example, under real outdoor atmospheric conditions, fluorinated polymer coated perovskite solar cells have been shown to exhibit very high stability, maintaining 96% of their initial PCE after 3 months whereas the uncoated reference device failed within 1 month even under only UV radiation and Ar atmosphere [135]. If the coating material acts as an energy down-converter for the PeLED, converting some of the emitted high energy blue luminescence to lower energy yellow-red light, this structure could simultaneously deliver a high quality white output. The introduction of low-dimensional perovskites into the 3D structure has been shown to possibly increase van der Waals interactions between the organic molecules and the perovskite lattice, thereby enhancing the structural stability. For instance, it has been demonstrated that solar cells based on 2D perovskite exhibits better photostability, retaining 70% of their initial PCE after 3 months compared to the 3D perovskite which degraded to 10% of their initial value [39]. Thus, the development of robust perovskite active layers is a top priority to improve the device stability. Furthermore, the incorporation of suitable cations or molecules that relaxes the lattice strain of the perovskite crystal structure can lead to an overall stabilization of the material.

The other challenge to overcome is replacing lead based perovskites with environmentally friendly alternatives. This motivation has already stimulated development of novel lead-free materials, such as methylammonium/cesium tin halide perovskites [137], methylammonium bismuth (III) halide perovskites [138] and double perovskite $Cs_2BiAgCl_6$ [139] as alternate light absorbers. Although the device performances of solar cells fabricated using these materials do not compare with those based on Pb-based

materials, they hold a high promise as a viable alternative. Therefore, the optoelectronic properties of these Pb-free halide perovskites need to be explored further for light emitting applications.

For electrically pumped laser devices, a much higher carrier injection is required in comparison to LEDs. In an optically pumped perovskite laser, the threshold of photon density to realize lasing is typically around 10^{11} cm^{-2}. From this, the minimum injection current density required to reach the lasing threshold for electrically pumped laser is estimated to be around 1000 A/cm^{-2}. This implies that under such extreme condition, thermal effects leading to lattice degradation and shortening of device lifetime need to be taken into consideration. Nurmikko and coworkers recently show that laser output of the perovskite laser device maintains its approximate original value for ≈4 h (total laser shots $> 10^7$) under the quasi-steady-state nanosecond pump conditions [140]. However, for commercial applications, longer laser lifetime is required. Therefore, since the consequence of short device lifetimes are mainly related to materials quality and stability under intense lasing conditions, thermal management and the proposed materials stabilization strategies outlined above should be tailored for operations under high lasing power.

In conclusion, metal-halide perovskites promise colorful and better light emitting applications given that they exhibit a broadly tunable bandgap. LEDs ranging from UV to NIR with pure color have been achieved and white light devices are plausible. They hold the key to a great and wide market in public, indoor and architectural solid-state lighting.

Acknowledgements

We apologize that many excellent papers were not included due to space constraints. We would like to acknowledge funding from the European Research Council (ERC Starting Grant 'Hy-SPOD' No. 306983) and the Foundation for Fundamental Research on Matter (FOM), which is part of the Netherlands Organization for Scientific Research (NWO), under the framework of the FOM Focus Group 'Next Generation Organic Photovoltaics'. S. Adjokatse acknowledges financial support from the NWO Graduate School funding.

References

[1] A. De Almeida, et al. Renew. Sustain. Energy Rev. 34 (2014) 30.
[2] N. Holonyak, et al. Appl. Phys. Lett. 1 (1962) 82.
[3] R.N. Hall, et al. Phys. Rev. Lett. 9 (1962) 366.
[4] H. Amano, et al. Appl. Phys. Lett. 48 (1986) 353.
[5] G.E. Höfler, et al. Electron. Lett. 34 (1998) 1781.
[6] M.R. Krames, et al. IEEE/OSA J. Disp. Technol. 3 (2007) 160.
[7] H.P. Maruska, et al. Mater. Res. Bull. 7 (1972) 777.
[8] C.W. Tang, et al. Appl. Phys. Lett. 51 (1987) 913.
[9] E. Bellmann, et al. Chem. Mater. 10 (1998) 1668.
[10] T.R. Hebner, et al. Appl. Phys. Lett. 72 (1998) 519.
[11] F.J. Duarte, et al. Opt. Lett. 30 (2005) 3072.
[12] J.H. Burroughes, et al. Nature 347 (1990) 539.
[13] J. Bharathan, et al. Appl. Phys. Lett. 72 (1998) 2660.
[14] W. Ki Bae, et al. Nanotechnology 20 (2009) 75202.
[15] W.K. Bae, et al. Adv. Mater. 21 (2009) 1690.
[16] W.K. Bae, et al. Nano Lett. 10 (2010) 2368.
[17] Y. Shirasaki, et al. Nat. Photonics 7 (2013) 13.
[18] X. Dai, et al. Nature 515 (2014) 96.
[19] B.S. Mashford, et al. Nat. Photonics 7 (2013) 407.
[20] G. Xing, et al. Nat. Mater. 13 (2014) 476.
[21] J. Wang, et al. Adv. Mater. 27 (2015) 2311.
[22] H. Cho, et al. Science 350 (2015) 1222.
[23] A. Sadhanala, et al. Nano Lett. 15 (2015) 6095.
[24] O.A. Jaramillo-Quintero, et al. J. Phys. Chem. Lett. 6 (2015) 1883.
[25] S. Pathak, et al. Chem. Mater. 27 (2015) 8066.
[26] R.L.Z. Hoye, et al. Adv. Mater. 27 (2015) 1414.
[27] Z.-K. Tan, et al. Nat. Nanotechnol. 9 (2014) 687.
[28] A. Kojima, et al. J. Am. Chem. Soc. 131 (2009) 6050.
[29] H.-S. Kim, et al. Sci. Rep. 2 (2012) 591.
[30] M.M. Lee, et al. Science 338 (2012) 643.
[31] J. Burschka, et al. Nature 499 (2013) 316.
[32] G.E. Eperon, et al. Energy Environ. Sci. 7 (2014) 982.
[33] J.H. Heo, et al. Nat. Photonics 7 (2013) 486.
[34] J.H. Noh, et al. Nano Lett. 13 (2013) 1764.
[35] N.J. Jeon, et al. Nat. Mater. 13 (2014) 897.
[36] W.S. Yang, et al. Science 348 (2015) 1234.
[37] Y. Liu, et al. Adv. Mater. 27 (2015) 5176.
[38] D. Shi, et al. Science 347 (2015) 519.
[39] H. Tsai, et al. Nature 536 (2016) 312.
[40] L. Protesescu, et al. Nano Lett. 15 (2015) 3692.
[41] Y. Hassan, et al. Adv. Mater. 28 (2016) 566.
[42] L.C. Schmidt, et al. J. Am. Chem. Soc. 136 (2014) 850.
[43] H. Zhu, et al. Nat. Mater. 14 (2015) 636.
[44] NREL, http://www.nrel.gov/ncpv/images/efficiency_chart.jpg (2016).
[45] F. Deschler, et al. J. Phys. Chem. Lett. 5 (2014) 1421.
[46] H. Wei, et al. Nat. Photonics 10 (2016) 333.
[47] S. Yakunin, et al. Nat. Photonics 9 (2015) 444.
[48] X.Y. Chin, et al. Nat. Commun. 6 (2015) 7383.
[49] M. Peng, et al. Sci. China Chem. 59 (2016) 653.
[50] S. Stranks, et al. Nat. Nanotechnol. 10 (2015) 391.
[51] S.A. Veldhuis, et al. Adv. Mater. 28 (2016) 6804.
[52] H. Huang, et al. NPG Asia Mater. 8 (2016) e328.
[53] P. Gao, et al. Energy Environ. Sci. 7 (2014) 2448.
[54] N. Pellet, et al. Angew. Chem. Int. Ed. 53 (2014) 3151.
[55] C.C. Stoumpos, et al. Inorg. Chem. 52 (2013) 9019.
[56] A. Sadhanala, et al. J. Phys. Chem. Lett. 5 (2014) 2501.
[57] F. Hao, et al. J. Am. Chem. Soc. 136 (2014) 8094.
[58] N. Kitazawa, et al. J. Mater. Sci. 37 (2002) 3585.
[59] J. Noh, et al. Nano Lett. 13 (2013) 1764.
[60] E.T. Hoke, et al. Chem. Sci. 6 (2015) 613.
[61] D.J. Slotcavage, et al. ACS Energy Lett. 1 (2016) 1199.
[62] A. Amat, et al. Nano Lett. 14 (2014) 3608.
[63] T. Umebayashi, et al. Phys. Rev. B 67 (2003) 155405.
[64] I. Borriello, et al. Phys. Rev. B 77 (2008) 235214.
[65] I.B. Koutselas, et al. J. Phys. Condens. Matter 8 (1996) 1217.
[66] J. Chang, et al. J. Mater. A 4 (2016) 887.
[67] Y. Chang, et al. J. Korean Phys. Soc. 44 (2004) 889.
[68] E. Mosconi, et al. J. Phys. Chem. C 117 (2013) 13902.
[69] J. Even, et al. J. Phys. Chem. Lett. 4 (2013) 2999.
[70] T. Baikie, et al. J. Mater. Chem. A 1 (2013) 5628.
[71] L. Huang, et al. Phys. Rev. B 88 (2013) 165203.
[72] F. Brivio, et al. APL Mater. 1 (2013) 042111.
[73] J.L. Knutson, et al. Inorg. Chem. 44 (2005) 4699.
[74] J.P. Correa Baena, et al. Energy Environ. Sci. 8 (2015) 2928.
[75] M. Saliba, et al. Energy Environ. Sci. 9 (2016) 1989.
[76] M.E. Kamminga, et al. Chem. Mater. 28 (2016) 4554.
[77] M. Yuan, et al. Nat. Nanotechnol. 11 (2016) 872.
[78] N. Wang, et al. Nat. Photonics 10 (2016) 699.
[79] H. Huang, et al. Adv. Sci. 2 (2015) 1500194.
[80] M.F. Aygüler, et al. J. Phys. Chem. C 119 (2015) 12047.
[81] F. Zhang, et al. ACS Nano 9 (2015) 4533.
[82] D. Zhang, et al. J. Am. Chem. Soc. 138 (2016) 7236.
[83] Q.A. Akkerman, et al. J. Am. Chem. Soc. 138 (2016) 1010.
[84] Y. Bekenstein, et al. J. Am. Chem. Soc. 137 (2015) 16008.
[85] Q. Zhou, et al. Adv. Mater. 28 (2016) 9163.
[86] X. Zhang, et al. Nano Lett. 16 (2016) 1415.
[87] S. Ye, et al. Mater. Sci. Eng. R: Rep. 71 (2010) 1.
[88] M.B. Johnston, et al. Acc. Chem. Res. 49 (2016) 146.
[89] M. Saba, et al. Nat. Commun. 5 (2014) 5049.
[90] H.-H. Fang, et al. Adv. Funct. Mater. 25 (2015) 2378.
[91] H.-H. Fang, et al. Light Sci. Appl. 5 (2015) e16056.
[92] S.D. Stranks, et al. Phys. Rev. Appl. 2 (2014) 34007.
[93] W. Zhang, et al. Nat. Commun. 6 (2015) 10030.
[94] E.M. Hutter, et al. J. Phys. Chem. Lett. 6 (2015) 3082.
[95] W.-J. Yin, et al. Appl. Phys. Lett. 104 (2014) 63903.

[96] W.-J. Yin, et al. J. Phys. Chem. C 119 (2015) 5253.
[97] X. Deng, et al. J. Phys. Chem. C 120 (2016) 2542.
[98] N.K. Noel, et al. ACS Nano 8 (2014) 9815.
[99] R.J. Stewart, et al. J. Phys. Chem. Lett. 7 (2016) 1148.
[100] F. Wang, et al. Adv. Mater. 28 (2016) 9986.
[101] H.-H. Fang, et al. Adv. Funct. Mater. 26 (2016) 4653.
[102] D.W. deQuilettes, et al. Nat. Commun. 7 (2016) 11683.
[103] E. Mosconi, et al. Energy Environ. Sci. 9 (2016) 3180.
[104] H.-H. Fang, et al. Sci. Adv. 2 (2016) e1600534.
[105] H. Huang, et al. ACS Appl. Mater. Interfaces 7 (2015) 28128.
[106] J. Pan, et al. J. Phys. Chem. Lett. 6 (2015) 5027.
[107] W. Zhang, et al. Nat. Energy 1 (2016) 16048.
[108] Y. Ling, et al. Adv. Mater. 28 (2016) 305.
[109] M. Saba, et al. ACS Nano 7 (2013) 229.
[110] M. Cadelano, et al. Adv. Opt. Mater. 3 (2015) 1557.
[111] C. Wehrenfennig, et al. Adv. Mater. 26 (2014) 1584.
[112] P.C. Findlay, et al. Phys. Rev. B 58 (1998) 12908.
[113] M. Era, et al. Appl. Phys. Lett. 65 (1994) 676.
[114] X. Hong, et al. Solid State Commun. 84 (1992) 657.
[115] T. Hattori, et al. J. Chem. Phys. Lett. 254 (1996) 103.
[116] K. Chondroudis, et al. Chem. Mater. 11 (1999) 3028.
[117] J. Byun, et al. Adv. Mater. 28 (2016) 7515.
[118] J. Li, et al. Adv. Mater. 27 (2015) 5196.
[119] J. Li, et al. J. Phys. Chem. Lett. 7 (2016) 4059.
[120] Y.H. Kim, et al. Adv. Mater. 27 (2015) 1248.
[121] H. Huang, et al. Chem. Sci. 7 (2016) 5699.
[122] B.R. Sutherland, et al. ACS Nano 8 (2014) 10947.
[123] B.R. Sutherland, et al. Adv. Mater. 27 (2015) 53.
[124] S. Yakunin, et al. Nat. Commun. 6 (2015) 8056.
[125] C. She, et al. Nano Lett. 14 (2014) 2772.
[126] M. McGehee, et al. Phys. Rev. B 58 (1998) 7035.
[127] M. Saliba, et al. Adv. Mater. 28 (2016) 923.
[128] Y. Jia, et al. Nano Lett. 16 (2016) 4624.
[129] S. Chen, et al. ACS Nano 10 (2016) 3959.
[130] Q. Zhang, et al. Nano Lett. 14 (2014) 5995.
[131] X. Liu, et al. Adv. Sci. 3 (2016) 1600137.
[132] H. Huang, et al. J. Phys. Chem. Lett. 7 (2016) 4398.
[133] W. Li, et al. Beilstein J. Org. Chem. 12 (2016) 1401.
[134] S. Yang, et al. Nat. Energy 1 (2016) 15016.
[135] F. Bella, et al. Science 354 (2016) 203.
[136] Z. Shi, et al. Nano Lett. 17 (2017) 313.
[137] T.C. Jellicoe, et al. J. Am. Chem. Soc. 138 (2016) 2941.
[138] R.L.Z. Hoye, et al. Chemistry 22 (2016) 2605.
[139] M.R. Filip, et al. J. Phys. Chem. Lett. 7 (2016) 2579.
[140] S. Chen, et al. Adv. Mater. (2017) 1604781.
[141] O. Vybornyi, et al. Nanoscale 8 (2016) 6278.
[142] J. Even, et al. J. Chem. Chem. C 118 (2014) 11566.
[143] A. Fu, et al. Nat. Mater. 14 (2015) 557.